○ SpringerPlus

RESEARCH

CrossMark

Hydrothermal derived nitrogen doped SrTiO$_3$ for efficient visible light driven photocatalytic reduction of chromium(VI)

Guanjie Xing, Lanxiao Zhao, Tao Sun, Yiguo Su[*] and Xiaojing Wang[*]

*Correspondence:
cesyg@imu.edu.cn;
wang_xiao_jing@hotmail.com
College of Chemistry
and Chemical Engineering,
Inner Mongolia University,
Hohhot, Inner Mongolia
010021, People's Republic
of China

Abstract

In this work, we report on the synthesis of nitrogen doped SrTiO$_3$ nanoparticles with efficient visible light driven photocatalytic activity toward Cr(VI) by the solvothermal method. The samples are carefully characterized by X-ray diffraction, scanning electron microscopy, transmission electron microscopy, UV–Vis diffuse reflectance spectroscopy and photocatalytic test. It is found that nitrogen doping in SrTiO$_3$ lattice led to an apparent lattice expansion, particle size reduction as well as subsequent increase of Brunner–Emmet–Teller surface area. The visible light absorption edge and intensity can be modulated by nitrogen doping content, which absorption edge extends to about 600 nm. Moreover, nitrogen doping can not only modulate the visible light absorption feature, but also have consequence on the enhancement of charge separation efficiency, which can promote the photocatalytic activity. With well controlled particle size, Brunner–Emmet–Teller surface area, and electronic structure via nitrogen doping, the photocatalytic performance toward Cr(VI) reduction of nitrogen doped SrTiO$_3$ was optimized at initial hexamethylenetetramine content of 2.

Keywords: Doping, Photocatalysis, Chromium(VI) reduction, Strontium titanate

Background

Hexavalent chromium (Cr(VI)) is a common pollutant detected in groundwater originated from excessively released of electroplating, pigment production and tanning of leather, etc. (Wang et al. 2013a). Cr(VI) has raised considerable attention because of its high toxic, intense mobility and strong teratogenic activity to human organisms. The World Health Organization (WHO) has stipulated that Cr(VI) concentration in drinking water should be below 0.05 ppm (Chen et al. 2011). Precipitation (Gheju and Balcu 2011), adsorption (Sun et al. 2014a, b), ion exchange (Edebali and Pehlivan 2010) and membrane separation (Hsu et al. 2013) as conventional techniques are commonly used to eliminate Cr(VI) from wastewater. Precipitation and adsorption processes are economic and effective, but only efficient when the Cr(VI) concentration is relatively high (Abyaneh and Fazaelipoor 2016; Hokkanen et al. 2016). Ion exchange is high-efficiency in general, but it is rather expensive to maintain and operate (Ali et al. 2015). Some even cause secondary pollution. For example, solvent extraction method could bring in organic pollutants, sulfide precipitator as common precipitator may be residual and

generate hydrogen sulfide (H_2S). In general, conventional techniques are either low efficiency or cost too much when they are applied to low Cr(VI) concentration in wastewater (Wang et al. 2012a; Huang and Huang 1996).

Semiconductor photocatalytic reduction technology has attracted a lot of attention in recent years (Miseki et al. 2008; Kato and Kudo 2002; Wang et al. 2009; Mu et al. 2011; Nakhjavan et al. 2012; Duo et al. 2015; Zhang et al. 2009). Semiconductor photocatalytic technology has a promising prospect for wastewater Cr(VI) removing because it is efficiency and inexpensive to maintain and operate without secondary pollution (Hu et al. 2014; Meichtry et al. 2014; Gherbi et al. 2013; Alanis et al. 2013). Strontium titanate ($SrTiO_3$) could be applied in Cr(VI) ion contaminant reduction with excellent photocatalyst performance, but it is only effective under ultraviolet irradiation which is about 4 % of the sunlight (Zheng et al. 2011). That is to say, strontium titanate is ineffective under visible light irradiation when applied to photocatalysis because it has a 3.2 eV band gap energy (Dong et al. 2012). Many leading groups also take advantage of the high bandgap. Li Ji group and Ib Chorkendorff group use $SrTiO_3$ and TiO_2 as protective window layers for Si photocathode during water splitting, and they achieve good result (Ji et al. 2015; Bae et al. 2016). Doping with nonmetal atoms to $SrTiO_3$ material could hoist the valence band edge and extend its optical absorption edge towards the visible light range, resulting in visible light driven photocatalytic activity (Sulaeman et al. 2011; Zou et al. 2012). The perovskite phases materials characteristics depend on the anionic composition to a large extent. Therefore, replacing oxygen with other anions, take nitrogen for example, can greatly influence the physicochemical property of the material. There are many reports about doping action including anionic dopant species and metals ions, and anionic doping could narrow the desired semiconductor band gap better than cation ions doping (Khan et al. 2002; Chen and Burda 2008).

In our work, nitrogen-doped $SrTiO_3$ powders are synthesized by hydrothermal method reaction. We take hexamethylenetetramine as doping sources and KOH as mineralizer to obtain the fine particles with excellent photocatalytic activity. The nitrogen doping effects on $SrTiO_3$ nanoparticles are fully studied in an attempt to investigate the microstructure, optical properties and the relevance to the improved photocatalytic activity toward chromium(VI) reduction.

Experimental section

Synthesis of nitrogen doped $SrTiO_3$ samples

Titanium tetraisopropoxide $Ti(OC_3H_7)_4$ and strontium nitrate $Sr(NO_3)_2\cdot4H_2O$ were used as starting materials, hexamethylenetetramine (HMT) as nitrogen source, and KOH as mineralizer. All of them were reagent grade and used without further purification. $SrTiO_3$ was prepared by hydrothermal method. $Ti(OC_3H_7)_4$ was dissolved in 10 mL 2-propanol firstly, $Sr(NO_3)_2$ aqueous solution was added to $Ti(OC_3H_7)_4$ propanol solution dropwise with continuously stirring. Then, 0–8 g of HMT and 20 mL of 2 M KOH aqueous solution were added to the suspension in turn. The solution was placed into a Teflon container with a stainless steel autoclave outside and then the solution was heated at 200 °C for 3 h in an oven. After that, the autoclave was cooled to room temperature naturally, the obtained powder was washed with distilled water and alcohol three times and dried in vacuum at 60 °C overnight (Sulaeman et al. 2010). The final samples

were labeled as pure $SrTiO_3$, N-$SrTiO_3$(0.5), N-$SrTiO_3$(1), N-$SrTiO_3$(2), N-$SrTiO_3$(3), N-$SrTiO_3$(4), N-$SrTiO_3$(5), N-$SrTiO_3$(6) and N-$SrTiO_3$(8) with the increased HMT content.

Sample characterization

X-ray power diffraction (XRD) was applied to characterize the purity and crystallinity of all our samples (D8 Advance Bruker X-ray diffractometer, CuKα radiation, $2\theta = 20$–80°). Transmission electron microscopy (TEM) was used to determine the morphology of the as-prepared samples (JEM-2010 apparatus, 200 kVA acceleration voltage). Diffusive reflectance UV–Vis spectrophotometer (Perkin-Elmer Lambda35) was employed to measure the samples UV–Vis absorption, $BaSO_4$ was taken as the reference sample. Barrett–Emmett–Teller (BET) technique was taken to determine the specific surface areas (Micromeritics ASAP 2000 Surface Area and Porosity Analyzer). X-ray photo spectrometer (XPS) analysis was employed for sample element state (ESCALab220i-XL). PGSTAT302 N potentiostat galvanostat Autolab electrochemical working station using a standard three-compartment cell was used for photoelectrochemical characteristics under 300 W Xe arc lamp ($\geq$420 nm). The fluorine-doped tin oxide (FTO) glasses (0.6 cm^2) were washed for 30 min using absolute ethanol with ultrasonication. 0.1 g sample mixed with 0.01 g Polyvinylidene fluoride (PVDF) and 0.5 mL N-methyl pyrrolidinone (NMP) were placed in an glass bottle under magnetic stirring for at least 8 h. Then the obtained mixtures were coated on the FTO glasses. Photocatalyst solution was coated onto the FTO glasses substrate by drop casting using 5 µL pipette tip, and 3 drops were enough. Then we use the pipette tip to smooth the film at room temperature in the air. Lastly, the coated FTO glasses were dried for 4 h at 60 °C in the air. Photocatalyst coated FTO glass, a piece of Pt sheet, an Ag/AgCl electrode and 0.5 M sodium sulfate were used as the working electrode, counter electrode, reference electrode and electrolyte, respectively.

Photocatalytic reactivity test

Disposal ability of Cr(VI) was evaluated through photo-reduction under 300 W mercury lamp with a filter ($\lambda \geq 400$ nm) irradiation in photochemical reactor. 50 mL 5 mg L^{-1} Cr(VI) solution with pH adjusted to ≈1 containing 30 mg photocatalyst was magnetically stirred during photocatalytic test. 4 mL suspension was sampled at selected intervals and centrifuged (10,000 rpm, 5 min). The content of Cr(VI) was determined using diphenylcarbazide colorimetrical method (Ma et al. 2014). The reduction efficiency of Cr(VI) was calculated according to the formula:

$$\eta = (C_0 - C_t)/C_0 \times 100\%$$

where η is the photocatalytic efficiency, C_0 is the initial concentration of Cr(VI), and C_t is the concentration of Cr(VI) after illumination (for time t).

Results and discussion

Figure 1 showed the XRD patterns of the as-prepared samples. It was clearly seen that all diffraction peaks of pure $SrTiO_3$ could be readily indexed to a well-crystallized perovskite phase of $SrTiO_3$ (JCPDS no. 01-074-1296). There were no peaks belonging to
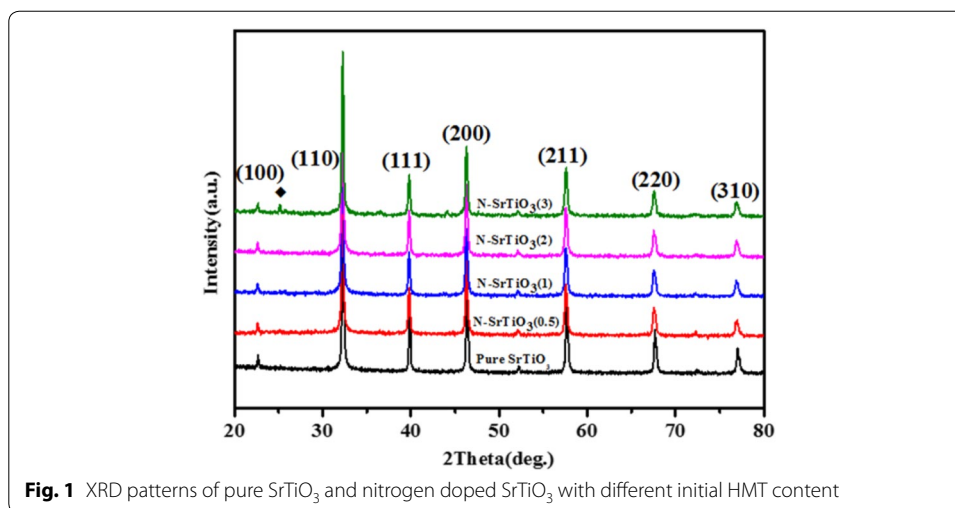
Fig. 1 XRD patterns of pure $SrTiO_3$ and nitrogen doped $SrTiO_3$ with different initial HMT content

other phases, indicating $SrTiO_3$ was phase pure. As for the nitrogen doped $SrTiO_3$ samples, it was observed that the diffraction peaks were identical to that of the pure $SrTiO_3$ except for the weakened intensity and narrowed full width at half maximum (FWHM) of the corresponding peaks with the increasing initial HMT content, suggesting a particle size reduction may occurred by the nitrogen doping action. It was noted that further increase of HMT content to 3.0 g led to the appearance of additional diffraction peaks belonging to $SrCO_3(2\theta = 25.15°, 25.79°)$ as shown in Fig. 1 and Additional file 1: Fig. S1. Structure refinement of the as prepared samples was carried out using general structure analysis system (GSAS) software (Larson and Von Dreele 1994). Rietveld refinement patterns of pristine $SrTiO_3$ and N-$SrTiO_3$ (2) samples were shown in Additional file 1: Fig. S2(a) and (b). The lattice parameters of pure $SrTiO_3$ and N-$SrTiO_3$(2) samples were listed in Additional file 1: Table S1. It was noted that the lattice volume of N-$SrTiO_3$ sample expanded from 59.676 to 60.043 Å^3. Several factors should be taken into consideration to clarify this phenomenon, including particle size, doping effect, surface feature, and so forth. Lattice expansion as a function of particle size reduction is not new and has been well documented in many semiconductors (Wang et al. 2013b; Mikhailovskaya et al. 2013). This can be ascribed to the surface structural relaxation due to the abundant surface exposed atoms. For the present $SrTiO_3$ samples, the primary particle size was estimated to be ~48 and 39 nm for pure $SrTiO_3$ and N-$SrTiO_3$(2) samples, respectively, from the diffraction peak (110) using Scherrer formula, indicating much large particle size, which was also verified by TEM observations. Basically, large particle size implies less surface exposed atoms, which leads to negligible variation of lattice parameters. On the other hand, doping effects will not only alter the lattice parameters and electronic structure, but also have consequence on the physical properties (Wang et al. 2013b; Mikhailovskaya et al. 2013). Nitrogen tends to occupy at the oxygen site in $SrTiO_3$ host matrix and results in lattice expansion because (1) the ionic radius of N^{3-} is 0.146 nm, which is a bit larger than 0.138 nm of O^{2-}, (2) Pauling's electronegativity of nitrogen is 3.04, which is close to that of 3.44 for oxygen. This conception can be further verified by XPS observations.
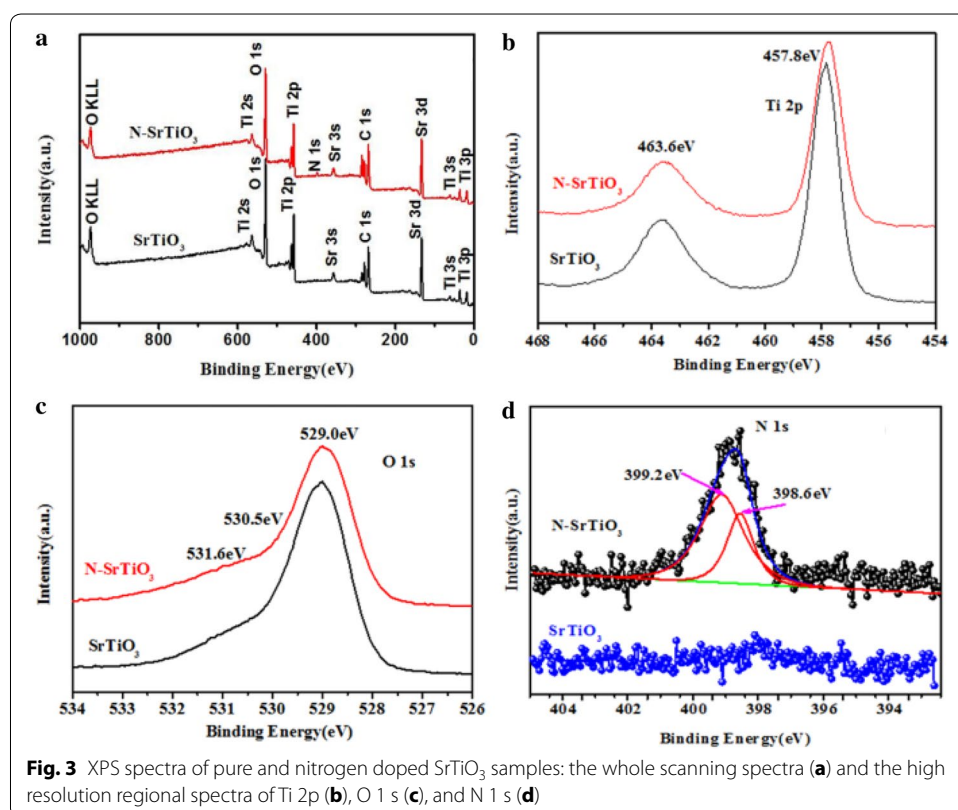
Transmission electron microscopy (TEM) was employed for samples morphology and crystal structure. Figure 2a showed the TEM image of pure $SrTiO_3$ nanoparticles. It can be seen that pure $SrTiO_3$ exhibited irregular cubic-like morphology with an average diameter of about 200 nm, which is larger than that obtained from XRD results. High resolution TEM (HRTEM) image indicated that pure $SrTiO_3$ exhibited high crystalline feature with the space between the adjacent of 0.2769 and 0.1931 nm, which was close to 0.276 and 0.194 nm for (110) and (200) plane of $SrTiO_3$, respectively (Fig. 2b). As for nitrogen doped samples, the diameter of N-$SrTiO_3$(2) showed a particle size reduction to ~100 nm with the same cubic-like morphology (Fig. 2c). HRTEM image for N-$SrTiO_3$(2) was shown in Fig. 2d. As illustrated in Fig. 2d, the lattice plane space was determined to be 0.2790 and 0.1603 nm, which is compatible to (110) and (211) plane for $SrTiO_3$.
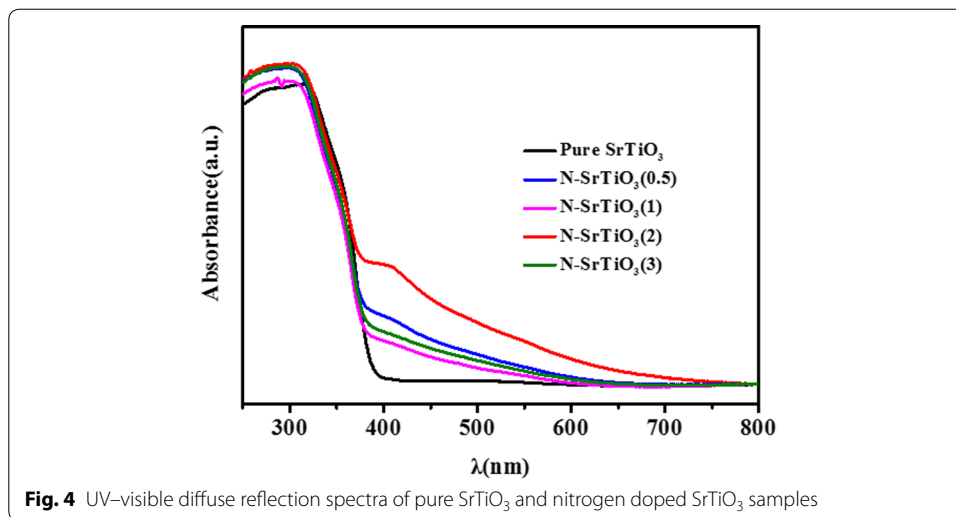
XPS technique was carried out to specify the chemical composition and charge state of the samples. Figure 3a shows the XPS global spectra of pure $SrTiO_3$ and N-$SrTiO_3$(2). From Fig. 3a, it was seen that all peaks can be ascribed to Sr, Ti, O, and C elements for pure $SrTiO_3$ and Sr, Ti, O, N and C for nitrogen doped $SrTiO_3$. Figure 3b showed the high resolution XPS spectra of Ti 2p for pure and nitrogen doped $SrTiO_3$. The binding energies of Ti $2p_{3/2}$ and Ti $2p_{1/2}$ appeared at about 457.6 and 463.4 eV, respectively, which is nearly identical to the typical values of $SrTiO_3$ (Sulaeman et al. 2011). Apparently, as shown in Fig. 3b, an about ~0.3 eV red shift was observed after the incorporation of

Fig. 2 TEM (**a**) and HRTEM (**b**) images of pure $SrTiO_3$, TEM (**c**) and HRTEM (**d**) images of N-$SrTiO_3$(2)
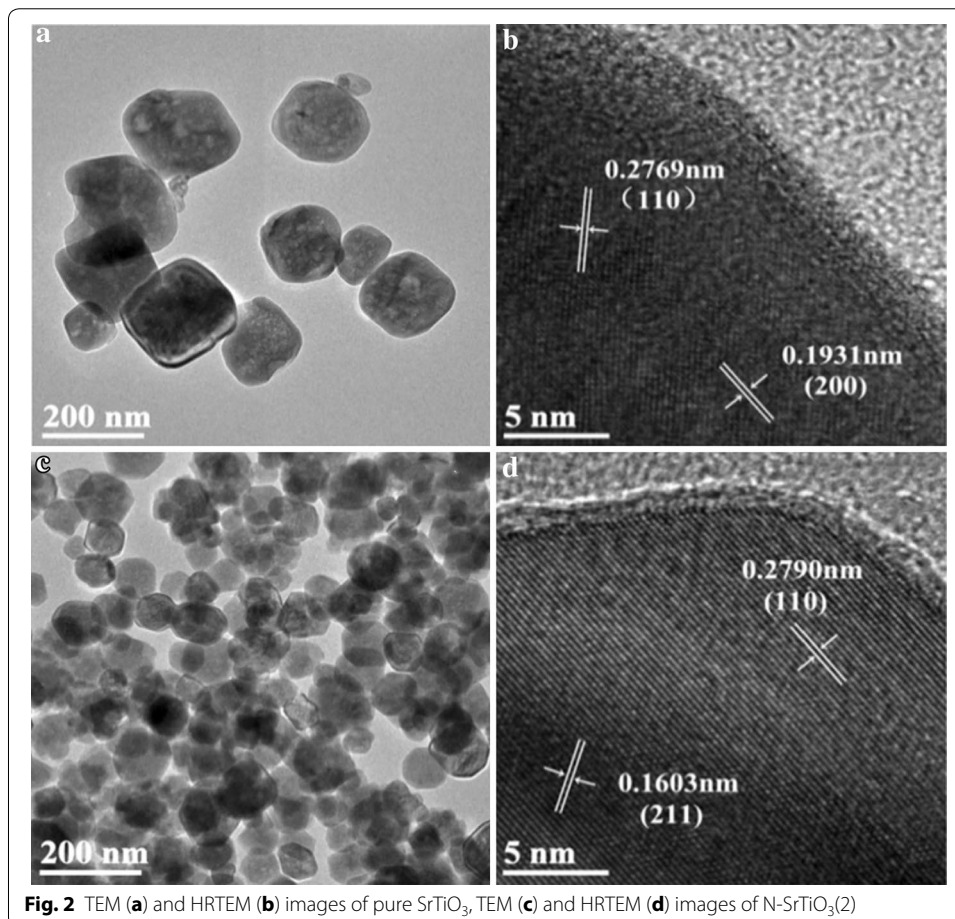
nitrogen. This observation is related to the fact that an increase of the electron density on Ti occurred because the electronegativity of the N atom is smaller than the O atom (Wang et al. 2012b). The O 1 s peak in the XPS spectra of pure $SrTiO_3$ and nitrogen doped $SrTiO_3$ was shown in Fig. 3c. The peaks appeared at 529.0, 530.5 and 531.6 eV, which can be ascribed to lattice oxygen atoms, surface hydroxyl groups and surface chemisorbed oxygen, respectively (Su et al. 2015). The N-species in the $N-SrTiO_3$ were displayed at 398.8 eV of N1 s XPS peak (Fig. 3d), which can be fitted into two peaks. The peak observed at binding energy of 399.2 eV was ascribed to sample surface adsorbed nitrogen while peak at 398.6 eV could be assigned to the shift of Ti–N bonds. The shift was very likely to be induced by the formation of O_{vac} and the Ti^{3+} cations adjacent to the vacancies (Zou et al. 2012).

The UV–Vis absorption performance of the samples was employed to investigate the electronic transitions and band gap energies of nitrogen doped $SrTiO_3$. As shown in Fig. 4, absorption edge of pure $SrTiO_3$ was about 386 nm, and the band gap energy was estimated to be 3.21 eV. Furthermore, a new absorption band at about 400–550 nm was observed in N-doped $SrTiO_3$ samples which may be resulted from N 2p to Ti 3d orbital electron transition. Interestingly, the absorption intensity of N-doped $SrTiO_3$ gradually increased with an increase of the initial HMT content. Moreover, the absorption edge also broadened to the higher wavelength more than 550 nm. It is presumed that the absorption above 550 nm is due to oxygen vacancy. When doping nitrogen into $SrTiO_3$, there was possibility that O^{2-} was replaced by N^{3-} which would result in anion defects for the charge compensation of O^{2-} and N^{3-} (Zou et al. 2012). Therefore, the formation

Fig. 3 XPS spectra of pure and nitrogen doped $SrTiO_3$ samples: the whole scanning spectra (**a**) and the high resolution regional spectra of Ti 2p (**b**), O 1 s (**c**), and N 1 s (**d**)

Fig. 4 UV–visible diffuse reflection spectra of pure $SrTiO_3$ and nitrogen doped $SrTiO_3$ samples
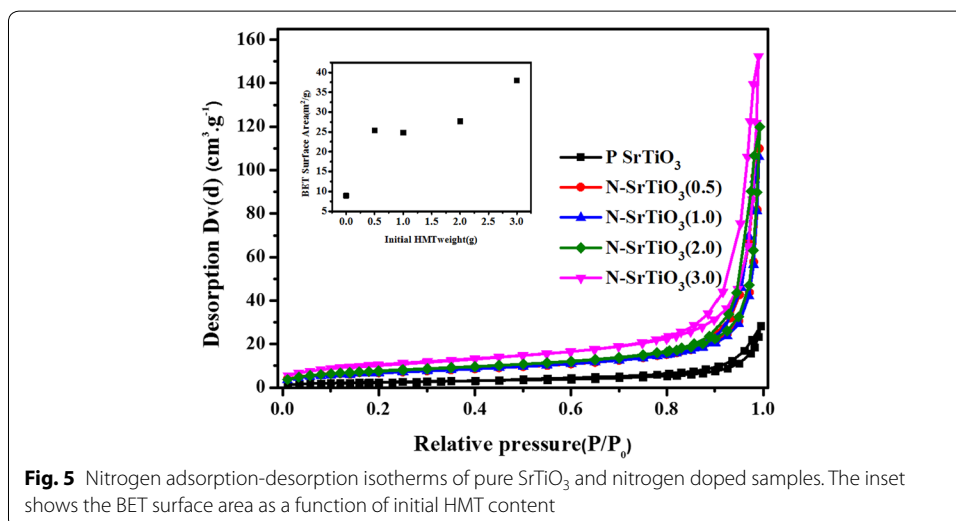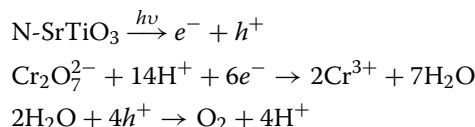
of the new band gaps in the visible light region could most possibly be ascribed to anion defects which were formed by nitrogen doping.

BET measurement was adopted to detect the impacts of nitrogen doping on surface areas of $SrTiO_3$. As shown in Fig. 5, the isotherm curves of $SrTiO_3$ samples with different nitrogen content were characterized by a hybrid type between type I and IV in the Brunauer Deming-Dming-Teller (BDDT) classification. It is worth noting that the BET surface area of pure $SrTiO_3$ nanoparticles is to be about 8.89 m^2/g, which, however, increases to ~37.94 m^2/g by nitrogen doping (inset of Fig. 5). The increase of surface area of the nitrogen doped $SrTiO_3$ nanoparticles may predict greatly enhanced photocatalytic activities.
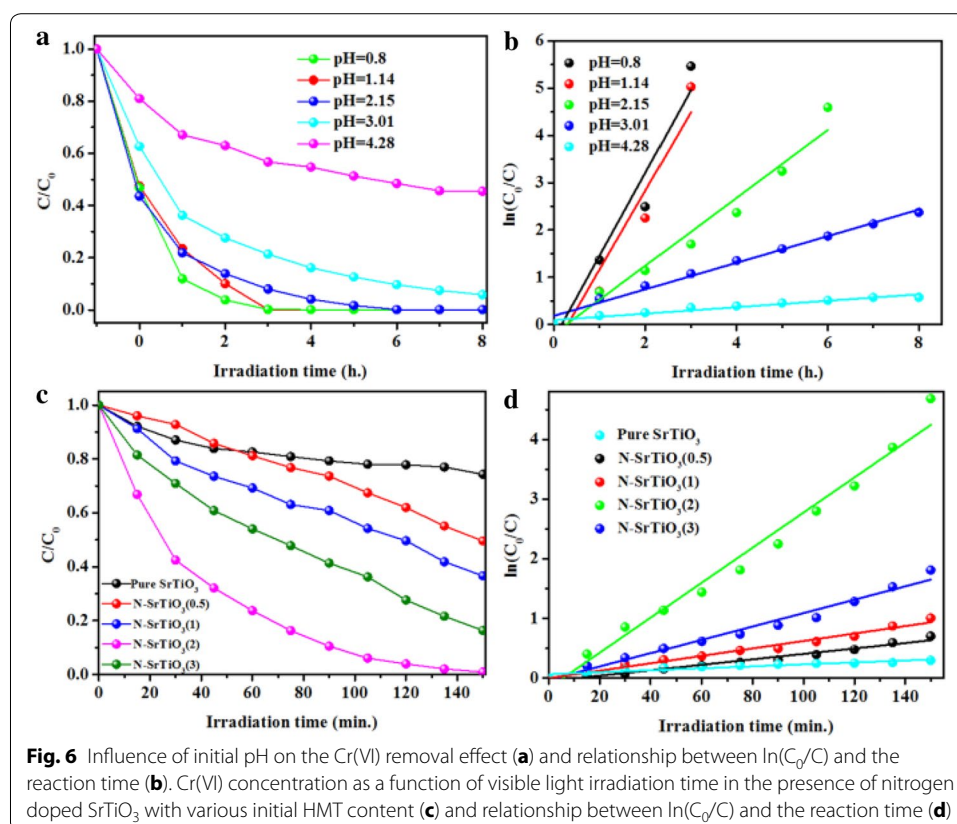
Cr(VI) reduction was used as the model reaction to investigate the doping effects of nitrogen on the photocatalytic performance of $SrTiO_3$. Cr(VI) suspensions were magnetically stirred to ensure the establishment of an adsorption/desorption equilibrium before illumination. Little Cr(VI) was adsorbed for all the as-prepared samples. Cr(VI)

Fig. 5 Nitrogen adsorption-desorption isotherms of pure $SrTiO_3$ and nitrogen doped samples. The inset shows the BET surface area as a function of initial HMT content

concentration was monitored using the standard diphenylcarbazide method with maximal adsorption at ~540 nm. The solution pH plays an important role on the reduction of Cr(VI). A series of experiments was conducted by varying solution pH from 0.5 to 4.3 to investigate pH influence. The pH influence of N-SrTiO$_3$(2) sample was presented in Fig. 6a. It was clear that the photocatalytic efficiency increased by degrees when adjust the initial pH from 4.28 to 0.5. The lower of the pH led to the higher of the photocatalytic efficiency. On the basis of other group's report, the relevant reactions during the reduction of Cr(VI) were as follows (Sun et al. 2014c; Mu et al. 2010):

$$\text{N-SrTiO}_3 \xrightarrow{h\upsilon} e^- + h^+$$
$$\text{Cr}_2\text{O}_7^{2-} + 14\text{H}^+ + 6e^- \rightarrow 2\text{Cr}^{3+} + 7\text{H}_2\text{O}$$
$$2\text{H}_2\text{O} + 4h^+ \rightarrow \text{O}_2 + 4\text{H}^+$$

It was seen that the higher H$^+$ concentration predicted higher reduction activity of Cr(VI) over nitrogen doped SrTiO$_3$. Thus, the photocatalytic reduction efficiency of Cr(VI) can be promoted at a lower pH condition. Considering the harm of low pH value to the facilities in application, we adopted pH≈1 in the later Cr(VI) reduction test. It is noted that there is a linear relationship between ln(C$_0$/C) and reaction time as seen in Fig. 6b, indicating the reduction of Cr(VI) proceeds through a pseudo-first-order kinetic reaction, ln(C$_0$/C) = k$_{app}$t, where k$_{app}$ is the apparent rate constant. The optimal apparent rate constant was determined to be 1.37 h^{-1} at pH value of 1. As seen in Fig. 6c, the

Fig. 6 Influence of initial pH on the Cr(VI) removal effect (**a**) and relationship between ln(C$_0$/C) and the reaction time (**b**). Cr(VI) concentration as a function of visible light irradiation time in the presence of nitrogen doped SrTiO$_3$ with various initial HMT content (**c**) and relationship between ln(C$_0$/C) and the reaction time (**d**)

photocatalytic performance of N-SrTiO$_3$ can be flexibly tuned by the initial HMT content. With the increase of the initial nitrogen content from 0 to 2 g, N-SrTiO$_3$ showed increasing photocatalytic activity and N-SrTiO$_3$(2) revealed the optimized photocatalytic activity. The reduction efficiency of 5 mg/L^{-1} Cr(VI) achieved to about 100 % after about 2 h under visible light irradiation. However, as for N-SrTiO$_3$(3) sample, there was a decrease in the photocatalytic performance. Moreover, the reduction of Cr(VI) proceeds through a pseudo-first-order kinetic reaction over all nitrogen doped SrTiO$_3$ samples as depicted in Fig. 6d. Two synergistic effects may be the reasons for the photocatalytic performance of the N-SrTiO$_3$ samples. One was that nitrogen doping action affected the surface feature of SrTiO$_3$ nanoparticles strongly. Doping action resulted in an increase of the specific surface area of the nitrogen doped SrTiO$_3$ samples which provided a better access for the Cr(VI) molecules to approach the as-prepared samples and then the Cr(VI) reduction reaction can easily proceed. Another factor is related to the band gap narrowing and efficient charge separation which was resulted from both N-dopants and the O$_{vac}$. Because of the O$_{vac}$, conduction band minimum (CBM) of nitrogen doped SrTiO$_3$ shifted more positive. At the same time, valence band maximum of nitrogen doped SrTiO$_3$ moved more negative for the reason of N-dopants (Zou et al. 2012). The efficient charge separation in nitrogen doped SrTiO$_3$ can be verified by Nyquist plot and photocurrent measurements. As shown in Fig. 7a, the observed arcs for both pure and
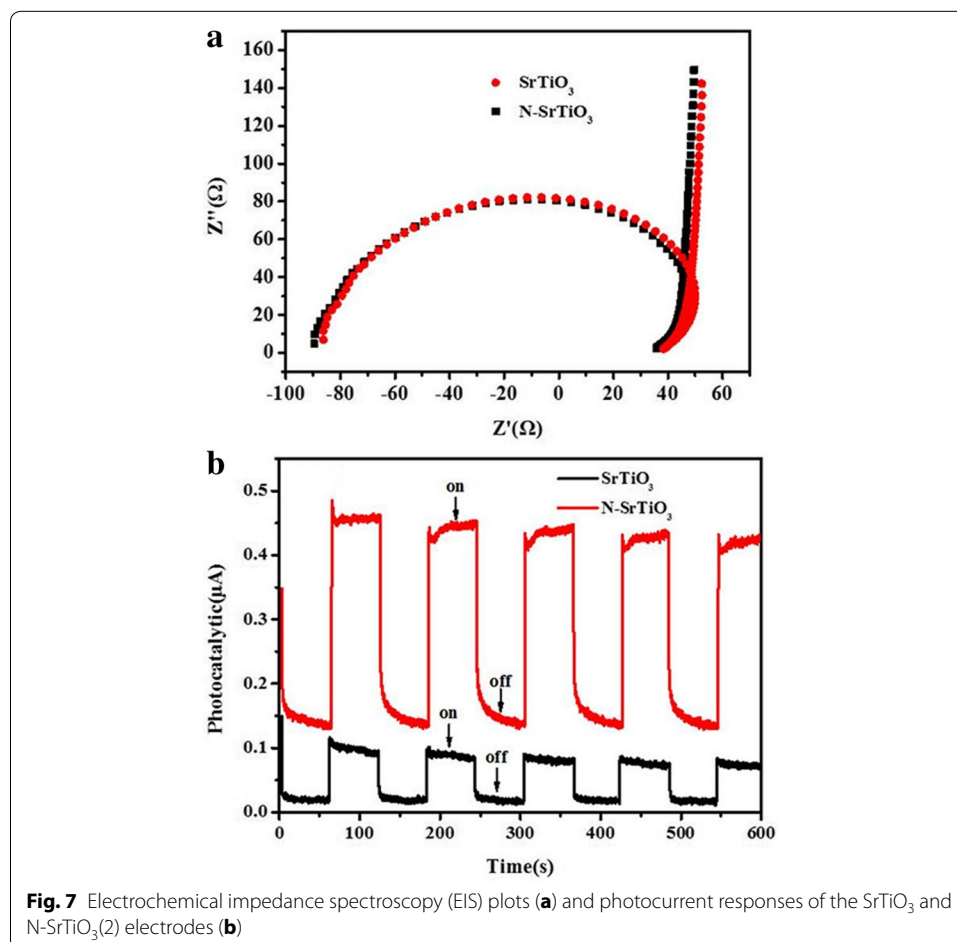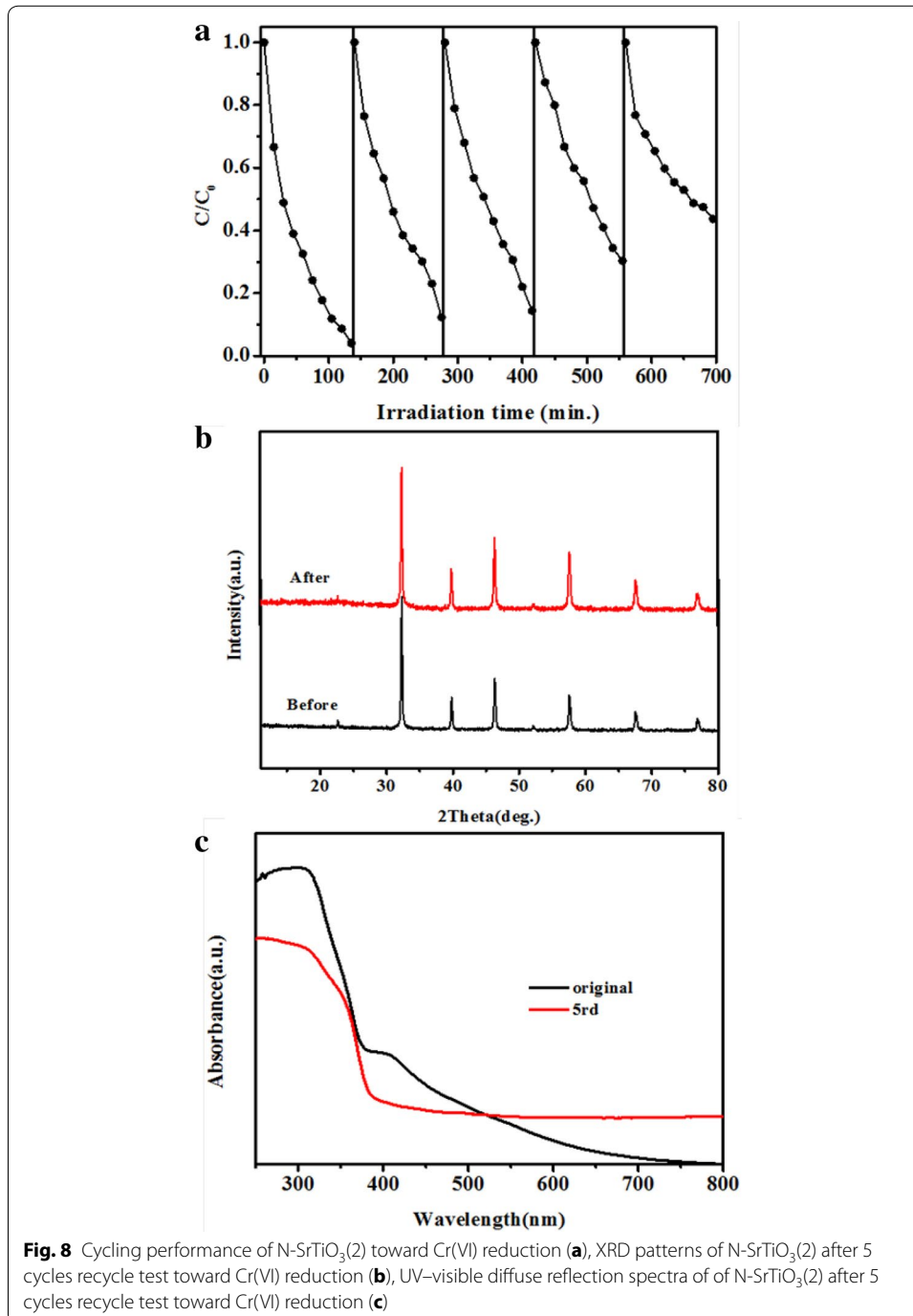

Fig. 7 Electrochemical impedance spectroscopy (EIS) plots (**a**) and photocurrent responses of the SrTiO$_3$ and N-SrTiO$_3$(2) electrodes (**b**)

nitrogen doped $SrTiO_3$ samples were depressed which was often observed in solid electrolytes impedance spectra. The arc radius on the Nyquist plot of $N-SrTiO_3$ electrode was almost the same with that of $SrTiO_3$ electrode. Generally speaking, photocurrent value could give an index to the sample's ability to generate and transfer the photogenerated charge carriers indirectly, which impact samples photocatalytic performance to a big degree (Dong et al. 2014). The photocurrent plots of the $SrTiO_3$ and $N-SrTiO_3$ electrodes under visible light was shown in Fig. 7b which was obtained at a bias voltage of

Fig. 8 Cycling performance of $N-SrTiO_3$(2) toward Cr(VI) reduction (**a**), XRD patterns of $N-SrTiO_3$(2) after 5 cycles recycle test toward Cr(VI) reduction (**b**), UV–visible diffuse reflection spectra of of $N-SrTiO_3$(2) after 5 cycles recycle test toward Cr(VI) reduction (**c**)

0.5 V. SrTiO$_3$ sample showed a photocurrent of 8.85×10^{-8} A while an enhanced photocurrent of 3.98×10^{-7} A for N-SrTiO$_3$ sample was observed at the same condition. The photocurrent for N-SrTiO$_3$ was nearly 4.5 times as much as the SrTiO$_3$ sample which indicated that the faster charge transfer and more effective separation of electron-hole pairs through the N-SrTiO$_3$ electrode interface, which can drastically enhance the photocatalytic activity toward Cr(VI) reduction.

To check the stability of the N-SrTiO$_3$(2) photocatalyst, recycle test was carried out. The XRD pattern and UV–visible diffuse reflection spectra of N-SrTiO$_3$(2) after the reduction of Cr(VI) was measured, and was shown in Fig. 8b, c. The XRD patterns peak of the N-SrTiO$_3$(2) sample did not change much before and after the Cr(VI) reduction test, suggesting that our photocatalyst was stable in structure. But as seen in Fig. 8c, visible light absorption decreased much after 5rd recycle test which may result from nitrogen loss in the nitrogen doped SrTiO$_3$, being often observed in several nitrogen doped oxides (Kumar et al. 2014; Ruzimuradov et al. 2015). This may also be the reason for decrease of photocatalytic performance in Fig. 8a as 55 % of the photocatalytic activity was preserved after 5 cycles. In summary, nitrogen doped SrTiO$_3$ possess excellent photocatalytic performance towards Cr(VI) reduction under visible light, but the stability of the nitrogen doped SrTiO$_3$ sample still needs to be further improved.

Conclusions

In summary, nitrogen doped SrTiO$_3$ nanoparticles with controlled particle size, electronic structure and efficient visible light driven photocatalytic activity toward Cr(VI) were successfully prepared by a solvothermal method. XRD, BET and TEM analyses indicated that nitrogen doped SrTiO$_3$ nanoparticles with cube-like morphology exhibited an apparent lattice expansion, particle size reduction as well as subsequent increase of BET surface area via nitrogen doping. The visible light absorption edge and intensity can be modulated by nitrogen doping content, which absorption edge extends to about 600 nm. Moreover, nitrogen doping can not only modulate the visible light absorption feature, but also have consequence on the enhancement of charge separation efficiency, which can promote the photocatalytic activity. With well controlled particle size, BET surface area, and electronic structure via nitrogen doping, the visible light driven photocatalytic performance toward Cr(VI) reduction of nitrogen doped SrTiO$_3$ was optimized at initial HMT content of 2. Such a finding may help to provide hints for developing and designing new photocatalytic semiconductors.

Additional file

Additional file 1. Supplementary data associated with this article.

References

Abyaneh AS, Fazaelipoor MH (2016) Evaluation of rhamnolipid (RL) as a biosurfactant for the removal of chromium from aqueous solutions by precipitate flotation. J Environ Manage 165:184–187

Alanis C, Natividad R, Barrera-Diaz C, Martínez-Miranda V, Prince J, Valente JS (2013) Photocatalytically enhanced Cr(VI) removal by mixed oxides derived from MeAl (Me: Mg and/or Zn) layered double hydroxides. Appl Catal B Environ 140–141:546–551

Ali SW, Mirza ML, Bhatti TM (2015) Removal of Cr(VI) using iron nanoparticles supported on porous cation-exchange resin. Hydrometallurgy 157:82–89

Bae D, Shayestehaminzadeh S, Thorsteinsson EB, Pedersen T, Hansen O, Seger B, Vesborg PCK, Ólafsson S, Chorkendorff I (2016) Protection of Si photocathode using TiO_2 deposited by high power impulse magnetron sputtering for H_2 evolution in alkaline media. Sol Energy Mater Sol Cells 144:758–765

Chen XB, Burda C (2008) The electronic origin of the visible-light absorption properties of C-, N-and S-Doped TiO_2 nano-materials. J Am Chem Soc 130:5018–5019

Chen H, Shao Y, Xu ZY, Wan HQ, Wan YQ, Zheng SR, Zhu DQ (2011) Effective catalytic reduction of Cr(VI) over TiO_2 nano-tube supported Pd catalysts. Appl Catal B Envrion 105:255–262

Dong WJ, Li XY, Yu J, Guo WC, Li BJ, Tan L, Li CR, Shi JJ, Wang G (2012) Porous $SrTiO_3$ spheres with enhanced photocatalytic performance. Mater Lett 67:131–134

Dong HJ, Sun JX, Chen G, Li CM, Hua YD, Lv CD (2014) An advanced Ag-based photocatalyst $Ag_2Ta_4O_{11}$ with outstanding activity, durability and universality for removing organic dyes. Phys Chem Chem Phys 16:23915–23921

Duo F, Wang Y, Mao X, Zhang X, Wang Y, Fan C (2015) A $BiPO_4$/BiOCl heterojunction photocatalyst with enhancedelec-tron-hole separation and excellent photocatalytic performance. Appl Surf Sci 340:35–42

Edebali S, Pehlivan E (2010) Evaluation of Amberlite IRA96 and Dowex 1 × 8 ion-exchange resins for the removal of Cr(VI) from aqueous solution. Chem Eng J 161:161–166

Gheju M, Balcu I (2011) Removal of chromium from Cr(VI) polluted wastewaters by reduction with scrap iron and subsequent precipitation of resulted cations. J Hazard Mater 196:131–138

Gherbi R, Trari M, Nasrallah N (2013) Influence of light flux and hydrodynamic flow regime on the photoreduction of Cr(VI) on the $CuAl_2O_4$/TiO_2 hetero-junction. Chem Eng 1:1275–1282

Hokkanen S, Bhatnagar A, Repo E, Lou S, Sillanpää M (2016) Calcium hydroxyapatite microfibrillated cellulose composite as a potential adsorbent for the removal of Cr(VI) from aqueous solution. Chem Eng J 283:445–452

Hsu HT, Chen SS, Tang YF, Hsi HC (2013) Enhanced photocatalytic activity of chromium(VI) reduction and EDTA oxidation by photoelectrocatalysis combining cationic exchange membrane processes. J Hazard Mater 248–249:97–106

Hu XF, Ji HH, Chang F, Luo YM (2014) Simultaneous photocatalytic Cr(VI) reduction and 2,4,6-TCP oxidation over g-C_3N_4 under visible light irradiation. Catal Today 224:34–40

Huang C, Huang CP (1996) Application of aspergillus oryzae and rhzopus oryzae for Cu(II) removal. Water Res 30:1985–1990

Ji L, McDaniel MD, Wang SJ, Posadas AB, Li XH, Huang HY, Lee JC, Demkov AA, Bard AJ, Ekerdt JG, Yu ET (2015) A silicon-based photocathode for water reduction with an epitaxial $SrTiO_3$ protection layer and a nanostructured catalyst. Nat Nanotechnol 10:84–90

Kato H, Kudo A (2002) Visible-light-response and photocatalytic activities of TiO_2 and $SrTiO_3$ photocatalysts codoped with antimony and chromium. J Phys Chem B 106:5029–5034

Khan SUM, Al-Shahry M, Ingler WB Jr (2002) Efficient photochemical water splitting by a chemically modified n-TiO_2. Science 297:2243–2246

Kumar S, Tonda S, Baruah A, Kumar B, Shanker V (2014) Synthesis of novel and stable g-C_3N_4/N-doped $SrTiO_3$ hybrid nanocomposites with improved photocurrent and photocatalytic activity under visible light irradiation. Dalton Trans 43:16105–16114

Larson AC, Von Dreele RB (1994) General structure analysis system (GSAS). Los Alamos National Laboratory Report LAUR, pp 86–748

Ma YL, Liu XQ, Li Y, Su YG, Chai ZL, Wang XJ (2014) $K_4Nb_6O_{17}$·4.5H_2O: a novel dual functional material with quick photore-duction of Cr(VI) and high adsorptive capacity of Cr(III). J Hazard Mater 279:537–545

Meichtry JM, Colbeau-Justin C, Custo G, Litter MI (2014) Preservation of the photocatalytic activity of TiO_2 by EDTA in thereductive transformation of Cr(VI). Studies by time resolved microwave conductivity. Catal Today 224:236–243

Mikhailovskaya ZA, Buyanova ES, Petrova SA, Morozova MV, Zhukovskiy VM, Zakharov RG, Tarakina NV, Berger IF (2013) Cobalt-doped $Bi_{26}Mo_{10}O_{69}$: crystal structure and conductivity. J Solid State Chem 204:9–15

Miseki Y, Kato H, Kudo A (2008) Water splitting into H_2 and O_2 over niobate and titanate photocatalysts with (111) plane-type layered perovskite structure. Energy Environ Sci 2:306–314

Mu RX, Xu ZY, Li LY, Shao Y, Wan HQ, Zheng SR (2010) On the photocatalytic properties of elongated TiO_2 nanoparticles for phenol degradation and Cr(VI) reduction. J Hazard Mater 176:495–502

Mu S, Long Y, Kang SZ, Mu J (2011) Surface modification of TiO_2 nanoparticles with a C60 derivative and enhanced photocatalytic activity for the reduction of aqueous Cr(VI) ions. Catal Commun 11:741–744

Nakhjavan B, Tahir MN, Natalio F, Panthofer M, Gao H (2012) Ni@Fe_2O_3 heterodimers: controlled synthesis and magnetically recyclable catalytic application for dehalogenation reactions. Nanoscale 4:4571–4577

Ruzimuradov O, Sharipov K, Yarbekov A, Saidov K, Hojamberdiev M, Prasad RM, Cherkashinin G, Riedel R (2015) A facile preparation of dual-phase nitrogen-doped TiO_2-$SrTiO_3$ macroporous monolithic photocatalyst for organic dye photo degradation under visible light. J Eur Ceram Soc 35(6):1815–1821

Su YG, Huang SS, Wang TT, Peng LM, Wang XJ (2015) Defect-mediated efficient catalytic activity toward p-nitrophenol reduction: a case study of nitrogen doped calcium niobate system. J Hazard Mater 295:119–126

Sulaeman U, Yin S, Sato T (2010) Solvothermal synthesis and photocatalytic properties of nitrogen-doped $SrTiO_3$ Nanoparticles. J Nanomater

Sulaeman U, Yin S, Sato T (2011) Visible light photocatalytic activity induced by the carboxyl group chemically bonded on the surface of $SrTiO_3$. Appl Catal B Environ 102:286–290

Sun XT, Yang LR, Li Q, Zhao JM, Li XP, Wang XQ, Liu HZ (2014a) Amino-functionalized magnetic cellulose nanocomposite as adsorbent for removal of Cr(VI): synthesis and adsorption studies. Chem Eng J 241:175–183

Sun YY, Yue QY, Mao YP, Gao BY, Gao Y, Huang LH (2014b) Enhanced adsorption of chromium onto activated carbon by microwave-assisted H_3PO_4 mixed with Fe/Al/Mn activation. J Hazard Mater 265:191–200

Sun Q, Li H, Zheng SL, Sun ZM (2014c) Characterizations of nano-TiO_2/diatomite composites and theirphotocatalytic reduction of aqueous Cr(VI). Appl Surf Sci 311:369–376

Wang DF, Kako T, Ye JH (2009) New Series of Solid-Solution Semiconductors (AgNbO3)1-x(SrTiO3)x with Modulated Band Structure and Enhanced Visible-Light Photocatalytic Activity. J Phys Chem C 113:3785–3792

Wang Q, Guan YP, Ren XF, Yang MZ, Liu X (2012a) Removal of low concentration Cr(VI) from aqueous solution by magnetic-fluids fixed bed using the high gradient magnetic separation. J Colloid Interf Sci 374:325–330

Wang DH, Jia L, Wu XL, Lu LQ, Xu AW (2012b) One-step hydrothermal synthesis of N-doped TiO_2/C nanocomposites with high visible light photocatalytic activity. Nanoscale 4:576–584

Wang L, Li XY, Teng W, Zhao QD, Shi Y, Yue RL, Chen YF (2013a) Efficient photocatalytic reduction of aqueous Cr(VI) over flower-like $SnIn_4S_8$ microspheres under visible light illumination. J Hazard Mater 244–245:681–688

Wang M, Liu Q, Che YS, Zhang LF, Zhang D (2013b) Characterization and photocatalytic properties of N-doped $BiVO_4$ synthesized via a sol-gel method. J Alloys Compd 548:70–76

Zhang L, Wong KH, Chen Z, Yu JC, Zhao J, Hu C, Chan CY, Wong PK (2009) AgBr-Ag-Bi_2WO_6 nanojunction system: a novel and efficient photocatalyst with double visible-light active components. Appl Catal A Gen 363:221–229

Zheng ZK, Huang BB, Qin XY, Zhang XY, Dai Y (2011) Facile synthesis of $SrTiO_3$ hollow microspheres built as assembly of nanocubes and their associated photocatalytic activity. J Colloid Interf Sci 358:68–72

Zou F, Jiang Z, Qin XQ, Zhao YX, Jiang LY, Zhi JF, Xiao TC, Edwards PP (2012) Template-free synthesis of mesoporous N-doped SrTiO3 perovskite with high visible-light-driven photocatalytic activity. Chem Commun 48:8514–8516